ELSEVIER

Controller design for a closed-loop micromachined accelerometer

Jonathan Soen[a,b,*], Alina Voda[b], Cyril Condemine[a]

[a]*Electronics and Information Technologies Laboratory (CEA-LETI-DCIS), 17 rue des Martyrs, 38054 Grenoble, France*
[b]*Automatic Control Laboratory of Grenoble (LAG), ENSIEG-INPG, BP 46, 38402 Saint Martin d'Hères, France*

Abstract

This paper presents control strategies for the design of a digital closed-loop micromachined accelerometer. The microsystem is composed of a mechanical part sensitive to the external acceleration, and a fully integrated electronic part devoted to the readout and control. A feedback control approach was used from the beginning of the sensor design in order to reach a good trade-off between circuit complexity and control requirements (inputs/outputs required for identification, sampling frequency, controller order, ...). The measurement performance is linked to the closed-loop sensitivity functions and a controller design based on a pole placement method with sensitivity functions shaping is proposed. Simulation results forecast excellent performance and this identification/controller design procedure was successfully applied to an early microsensor prototype.
© 2006 Elsevier Ltd. All rights reserved.

1. Introduction

Micro electro mechanical systems (MEMS)-based sensors are finding an increasing number of applications in various fields such as medical systems, automotive industry, human/machine interfaces, etc. Most measurement principles have been adapted to MEMS-based microsystems. Sensor interfaces have also changed, with electronics being integrated as close as possible to the sensing element. Today, sensors are devices composed of the sensing element, pick-up electronics, signal processing and digital outputs.

In particular, micromachined acceleration sensors are now widely used. Although their development has been mainly driven by the automotive industry, for safety and riding comfort enhancement, other applications for motion capture and control are numerous (Yazdi, Ayazi, & Najafi, 1998).

The advantages of capacitive sensing and surface micromachining for the acceleration sensing part are now well established, as well as the advantages of $\Sigma\Delta$ switched-capacitor interfaces for direct readout and analog to digital conversion.

Although most of the commercial accelerometers operate in open-loop, closed-loop architectures which include the physical sensing element, a readout circuit and a compensator in a $\Sigma\Delta$ loop have been investigated in the recent years (Chau et al., 1996; Kraft, 1997). Indeed, closed-loop operation brings several advantages. In particular, it reduces or eliminates some recurrent problems in open-loop measurement systems, such as offsets and signal distortion due to nonlinear elements, while it potentially improves quantization noise shaping, measurement dynamic range and sensitivity. In counterpart, special care must be taken concerning the design of the sensor loop architecture and, in particular, the controller. Indeed, measurement performance trades-off with loop stability and robustness in this kind of sensor system and therefore designing a stable and robust sensor, with very high measurement performance, is a challenging problem.

*Corresponding author. Tel.: +33 4 38 78 24 87; fax: +33 4 38 78 90 73.
E-mail addresses: jonathan.soen@cea.fr (J. Soen),
Alina.Voda@inpg.fr (A. Voda), ccondemine@cea.fr (C. Condemine).

A detailed study already presents a controller design using μ-synthesis for a tunneling accelerometer (Liu, Rockstad, & Kenny, 1999). However, the sensing principle and the system characteristics differ, as well as the controller implementation. At present, to the authors' knowledge, there is no detailed study presenting an advanced control strategy applied to the design of a fully integrated control circuit for a capacitive micromachined accelerometer with digital output.

In this work, the acceleration sensing problem in closed-loop has been reformulated into a control problem. Initial measurement performance specifications (quantization noise shaping, accuracy, linearity) have been turned into control performance specifications (disturbance and noise rejection, closed-loop bandwidth). The proposed closed-loop architecture includes a digitally implemented programmable controller. The controller design is based on a *plant* model obtained by identification. Identification of the plant model (including mechanical and electronic parts) is essential during the prototyping step. Indeed, small variations in the MEMS fabrication process or in the settings of the electronic part (clock frequency, feedback or sensing voltages, offsets) can have a great influence on the system behavior. Performance and stability requirements are expressed by means of constraints on the shape of the closed-loop sensitivity functions. Controller design methodology is based on pole placement and sensitivity function shaping (Landau, Lozano, & M'Saad, 1997).

The open-loop/closed-loop measurement systems and associated block diagrams are presented in Section 2. The control problem formulation and the control performance specifications are exposed in Section 3. Section 4 presents the identification process applied to the physical model, the controller design methodology and the expected performance. Section 5 presents identification and controller design performed on the real microsensor.

2. System overview

The proposed implementation of the closed-loop acceleration sensor is briefly described in Fig. 1. This figure also displays a classical implementation of an open-loop integrated capacitive acceleration measurement system with digital output. Although both open-loop and closed-loop systems will be further detailed, the two measurement principles may be summarized as follows. In the open-loop system, the acceleration imposed to the sensor translates into an inertial force, which acts on a movable proof mass. The *proof mass displacement* is therefore a *measure* of the external acceleration. This displacement is read by a capacitive position sensing circuit. In the closed-loop system, the inertial force is *rebalanced* by the electrostatic force and the proof mass displacement is minimized. The *electrostatic actuation control signal* constitutes the sensor *measurement signal*.

The goal of this study is to propose a controller design leading to a digital acceleration sensor which achieves the high measurement performance stated in Table 1. The definitions and values of the main parameters, frequencies and time notations used in this article are gathered in Table 2.

2.1. Open-loop system

The micromachined accelerometer (Fig. 2) is fabricated on a SOI substrate. It is composed of a movable proof mass m maintained in its rest position ($x = 0$) by two suspension beams with mechanical stiffness k_{mec}. The proof mass displacement $x(t)$ under external acceleration $\gamma(t)$ can be approximated by the equation of a low-pass damped mass-spring system, so that mass displacement is proportional to the acceleration (for input frequencies below the device's cutoff frequency).

Two variable sense capacitances $C_1(x, t)$ and $C_2(x, t)$ are formed between the interdigitated comb fingers of the fixed
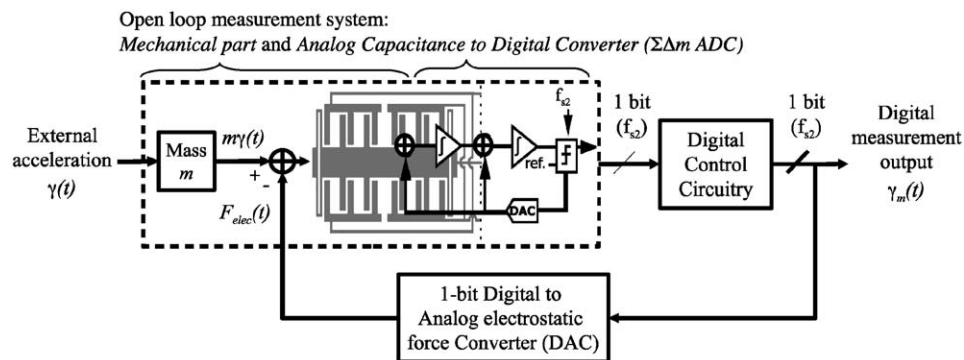

Fig. 1. Open-loop/closed-loop measurement systems: the comb capacitances of the micromachined accelerometer are integrated (switched capacitors) in the first stage of the readout $\Sigma\Delta$ modulator for a direct capacitance to digital conversion, which is represented as an analog $\Sigma\Delta$ modulator superposed on the micromachined accelerometer (open-loop system inset). The closed-loop measurement system is performed thanks to a digital integrated circuit and electrostatic force feedback.

Table 1
Sensor system initial specifications

Characteristic	Requirements
Sensor output	Digital ($\Sigma\Delta$)
Measurement full scale	$\gamma_{max} = \pm 10g$
Measurement bandwidth (MBW)	$0 - 122$ Hz
Measurement accuracy	$\leqslant -100$ dB
Measurement linearity	$THD \leqslant -100$ dB
Digital resolution on MBW	$SQNR \geqslant 100$ dB
Resulting $SNDR$	$SNDR \geqslant 100$ dB
Temperature range	$0 - 85\,°C$
Pressure range	$0.8 - 1.2$ atm

Table 2
System parameters, frequencies and time notations

Symbol	Description (Value *unit*)
m	Proof mass (1.214×10^{-7} kg)
b	Damping coefficient (4.583×10^{-4} N s m^{-1})
k_{eff}	Effective stiffness (4.79 N m^{-1})
K_u	Actuation gain (9.814×10^{-6} m^2 N^{-1} V^{-1})
K_{cs}	Capacitive readout gain (1.1295×10^6 m^{-1})
K_{csNL}	Capacitive readout nonlinear term (1.1521×10^{18} m^{-1})
x_{max}	Steady-state open-loop mass displacement for
	γ_{max} (0.833×10^{-6} m)
E_f	Quantization noise power spectral density (PSD)
	(2.36×10^{-4} dB$\sqrt{\text{Hz}}^{-1}$)
g	Acceleration due to gravity (9.807 m s^{-2})
f_1	Measurement bandwidth (122 Hz)
f_2	Mechanical natural frequency ($\simeq 1772$ Hz)
f_2'	Effective open-loop natural frequency ($\simeq 993$ Hz)
f_3	Closed-loop natural frequency ($\simeq 993$ Hz)
f_{s_1}	Controller sampling frequency (62.5 kHz)
k_1, q_1^{-1}	Sample number and delay operator for f_{s_1}
f_{s_2}	Filters and $\Sigma\Delta$ modulators sampling frequency (250 kHz)
k_2, q_2^{-1}	Sample number and delay operator for f_{s_2}

electrodes and those of the movable proof mass. The variations of these capacitances are read by an appropriate circuit, which consists of a switched capacitor interface integrated in a 2nd order $\Sigma\Delta$ modulator. Thanks to a readout voltage V_r of particular wave form applied to both electrodes (Fig. 2), this interface performs a direct conversion from capacitance to digital signal (Wang, Kajita, Sun, & Temes, 1998).[1] The open-loop measurement system is given in Fig. 3, where *STF* (resp., *NTF*) stands for the signal (resp., noise) transfer function of the $\Sigma\Delta$ modulator.

Considering the sensor design, the conversion from mass position $x(t)$ to the normalized differential capacitance signal $\Delta C_{norm}(x,t)$ can be approximated by the nonlinear relation (1):

$$\Delta C_{norm}(x,t) \simeq K \cdot x(t) + K_{NL} \cdot x^3(t) + o(x^4), \qquad (1)$$

[1]$\Sigma\Delta$ conversion is well adapted to sensor interfaces. It performs a very high resolution conversion with reduced analog electronics.

where K_{cs} and K_{csNL} are defined in Table 2. The $o(.)$ term stands for the negligible higher order terms.

The cubic nonlinearity introduces distortions which affect the measurement signal to noise and distortion ratio (SNDR). Fig. 4 plots the achievable SNDR versus normalized mass displacement x/x_{max} for the open-loop system. This plot shows that, in order to comply with the system specification for SNDR (Table 1), the mass displacement should be kept around 1% of the maximal open-loop displacement x_{max}. A first solution would be to restrict proof mass displacement using stiffer suspension beams. However, this reduces the sensor sensitivity and makes the capacitive position sensing circuit harder to design. Another solution is to design a closed-loop measurement system using electrostatic feedback actuation.

2.2. Electrostatic feedback actuation, readout voltage and mass dynamics

Feedback actuation is performed by means of a high frequency (f_{s_2}) on–off-type electrostatic actuation. When the proof mass is away from its rest position, a constant voltage difference V_{fb} (Fig. 2) is applied between the appropriate fixed electrode and the movable proof mass. This creates an attractive electrostatic force F_{elec} which moves the proof mass back toward the rest position. The electrode selection signal, which also constitutes the closed-loop sensor output, is given by the output of a second order digital $\Sigma\Delta$ modulator, imbedded in the digital control circuitry. This second $\Sigma\Delta$ modulator operates at a sampling frequency $f_{s_2} = 250$ kHz and is fed by the controller output $u(k_1)$ sampled at $f_{s_1} = 62.5$ kHz, thanks to a frequency adaptation block detailed later. The same electrodes are used for position sensing and feedback actuation. Readout voltage and electrostatic actuation voltage have a particular effect on the MEMS frequency behavior. Using $\Sigma\Delta$ signal properties, averaging and linearization methods, the total electrostatic force can be approximated by

$$F_{elec}(u,x,t,k_1) = K_u \cdot u(k_1) - k_{elec} \cdot x(t) + o(x^2, u^2), \qquad (2)$$

where k_{elec} is called electrostatic stiffness, K_u is the actuation gain, $u(k_1)$ is the control signal and k_1 is the sample number associated to control signals. The approximate mass motion equation is given in (3), which results in (4), according to (2)

$$m \cdot \ddot{x}(t) + b \cdot \dot{x}(t) + k_{mec} \cdot x(t) = m \cdot g \cdot \gamma(t) + F_{elec}(\ldots), \quad (3)$$

$$m \cdot \ddot{x}(t) + b \cdot \dot{x}(t) + k_{eff} \cdot x(t) = m \cdot g \cdot \gamma(t) + K_u \cdot u(k_1), \qquad (4)$$

where

$$k_{eff} = k_{mec} + k_{elec}. \qquad (5)$$

In these equations, the electrostatic stiffness k_{elec} is negative, so that the system's effective stiffness k_{eff} will be smaller than the mechanical stiffness k_{mec}. This
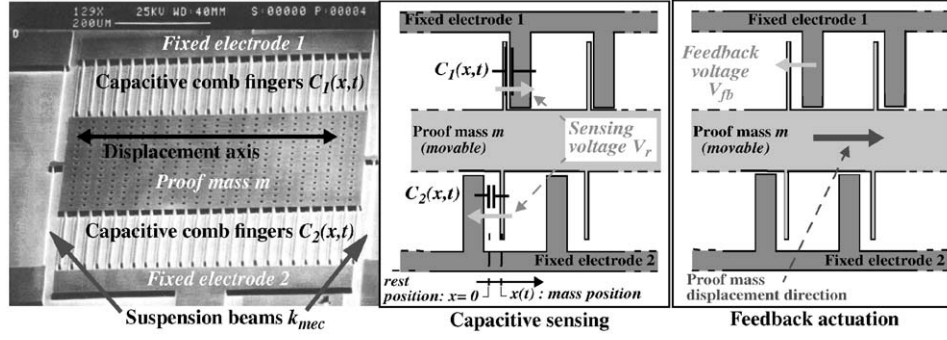
Fig. 2. Scanning electron microscope view of the MEMS capacitive accelerometer and illustrations of capacitive sensing and feedback actuation.
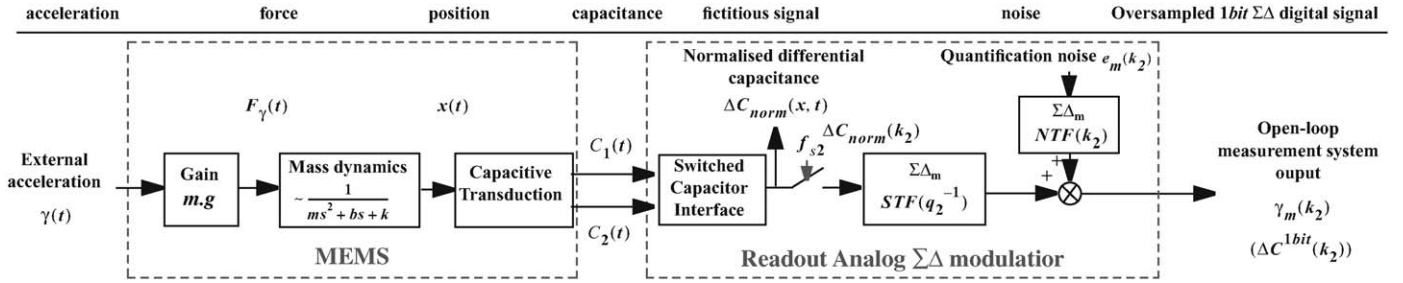

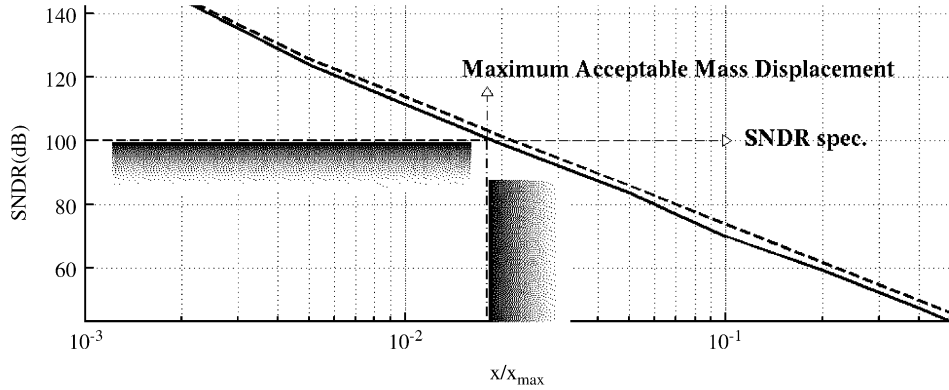Fig. 3. Detailed diagram of the open-loop measurement system.

Fig. 4. Achievable SNDR versus amplitude of mass displacement x: harmonic distortion contribution (solid line) and distortion products contribution (dashed line).

phenomenon, known as electrostatic stiffness softening (Handtmann, Aigner, Meckes, & Wachutka, 2002), will lead to a reduction of the sensor's effective natural frequency f_2', compared to its mechanical natural frequency f_2. The damping coefficient b is mainly due to the air squeezed film effect between interdigitated comb fingers (Senturia, 2001). Considering the operating conditions and the MEMS design, the spring effect of the squeezed film is assumed to be negligible. The damping coefficient's non-linear dependence on mass position $x(t)$ is also assumed to be negligible (when the system operates in closed-loop) compared to uncertainties on its value and its variation with temperature. Finally, the approximate transfer function from the control signal $u(k_1)$ to the mass displacement

$x(t)$ will be

$$G_{th}(s) = \frac{X(s)}{U^*(s)} = \frac{K_u}{m \cdot s^2 + b \cdot s + k_{eff}}, \qquad (6)$$

where $U^*(s)$ is the starred Laplace transform of $u(k_1)$. The denominator will be further referred to as the *mass dynamics* in the closed-loop structure (Fig. 5).

2.3. Control circuitry architecture design

Two main feedback control considerations have oriented the design of the integrated circuit architecture. The first one is that a controller design based on the physical plant model will not be robust. Indeed, MEMS fabrication is
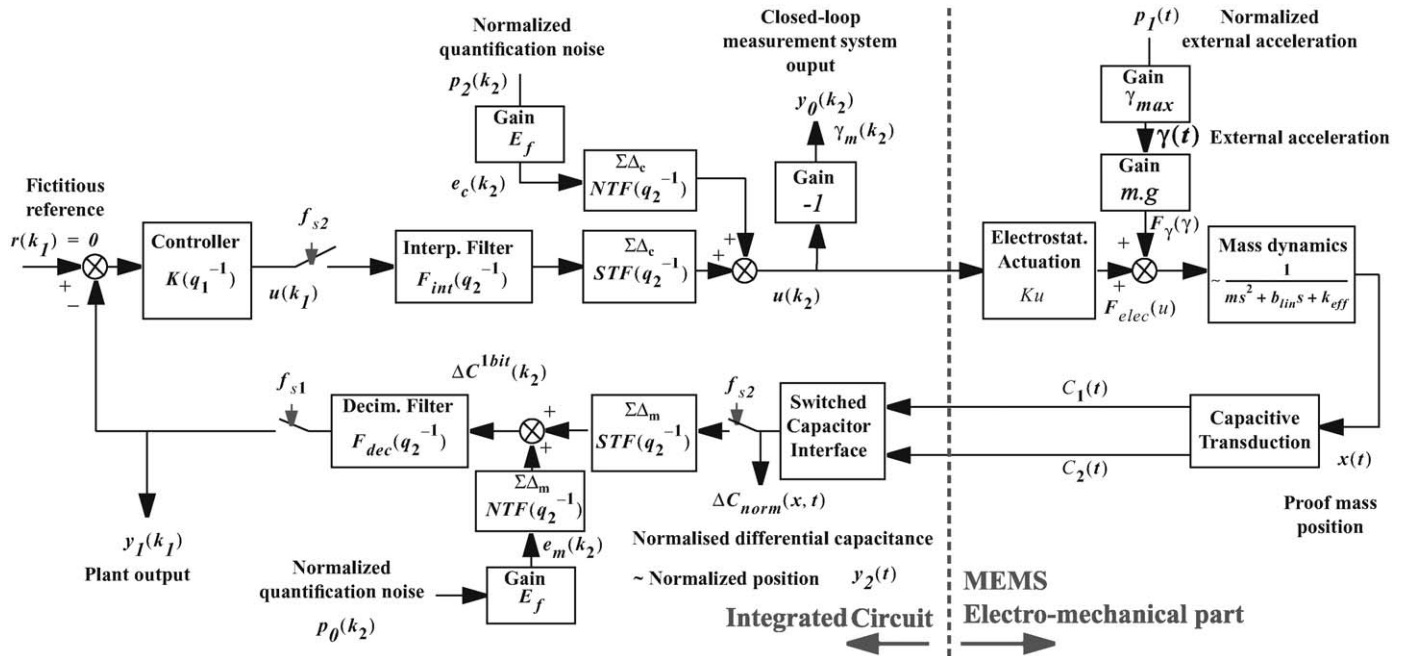
Fig. 5. Detailed diagram of the closed-loop system.

subject to technological dispersions. Parameter values, such as mass, damping or mechanical/effective stiffness coefficients, might be very different from the expected ones, especially in the prototyping step. To alleviate this problem of expected/effective behavior mismatch, the designed integrated circuit allows plant identification and includes a programmable digital controller. During the prototyping step, a new controller can be designed and optimized for each produced sensor. Later, once the technological process is established, the uncertainties on parameter values are evaluated so that a fully robust controller design may be realized for all produced sensors.

The second consideration is that, although $\Sigma\Delta$ conversion is well adapted to sensor interfaces, the oversampled nature of the $\Sigma\Delta$ signals is a problem for control purposes. Indeed, for the identification and the controller design, the suitable sampling frequency (f_{s_1}) must be at maximum 30 kHz.[2] However, the readout and actuation $\Sigma\Delta$-modulators have to work at $f_{s_2} = 250$ kHz for noise shaping requirements.[3] In order to deal with both frequencies, down and up sampling blocks (decimation and interpolation filters) have been introduced. Unfortunately, electronics design complexity as well as silicon area and therefore

the circuit's cost increase with the frequency ratio f_{s_2}/f_{s_1}, so that the constraint on the controller sampling frequency has been relaxed. The trade-off was to introduce third order decimation and interpolation filters. This choice led to a controller sampling frequency equal to $f_{s_1} = f_{s_2}/4 = 62.5$ kHz. The detailed diagram of the closed-loop system is given in Fig. 5. The plant to be controlled is defined as the system between the controller output $u(k_1)$ and the measured proof mass position $y_1(k_1)$.

3. Closed-loop system analysis

In this paper, the acceleration microsensor is treated from the feedback control point of view. This section translates the initial sensor system block diagram (Fig. 1) into an appropriate feedback control block diagram (Fig. 6). Then, initial measurement specifications and control requirements are expressed by means of constraints on the closed-loop sensitivity functions.

3.1. Control problem formulation

The control problem can be formulated as a tracking problem: the measured acceleration tracks the unknown external acceleration (see Fig. 1). It can also be formulated as a servo control problem (disturbance rejection problem). Indeed, the controller maintains the proof mass in its rest position ($x = 0$) despite the external acceleration. In other words, the inertial force induced by the external acceleration is considered here as a disturbance which is rejected by applying the opposite electrostatic force. The complete block diagram associated to this servo problem is shown in Fig. 5. Considering the reference $r(k_1) = 0$, the controller

---

[2]The sampling frequency should be between 20 and 30 times the plant's lowest dynamic for an efficient identification and between 6 and 25 times the closed-loop bandwidth for control purposes. Considering the effective natural frequency of the system ($f'_2 \simeq 1$ kHz), a sampling frequency f_{s_1} inferior to 30 kHz should be chosen.

[3]The target for the maximal signal to quantization noise ratio (SQNR) is 100 dB. This implies that the oversampling ratio (OSR) of the second order $\Sigma\Delta$ modulator must be equal to 1024. Since the desired measurement bandwidth (MBW) is 122 Hz, the oversampling frequency must be equal to 250 kHz ($OSR \times MBW \times 2$).
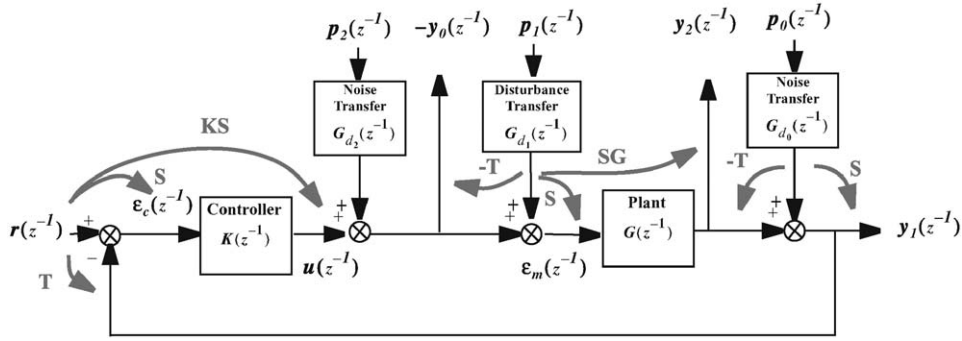
Fig. 6. Block diagram of the closed-loop system.

will force the plant output $y(k_1)$ to remain close to the null value (rest position $x = 0$). The measurement output $\gamma_m(k_2)$ results as the opposite of the resampled controller output $u(k_2)$. The servo control problem is treated in this paper.

The complete system (Fig. 5) can thus be modeled as a standard feedback loop with linear transfers (Fig. 6). This representation is valid since the mass displacement $x(t)$ is kept small by feedback. In this block diagram, all input and output signals are normalized. The sampling frequency of all signals and transfers corresponds to the controller sampling frequency f_{s_1}. Sample number k_1 and delay operator q_1 have been replaced by the z-transform notation z^{-1}. Some of the transfer functions are known ($G_{d_0}(z^{-1})$, $G_{d_1}(z^{-1})$ and $G_{d_2}(z^{-1})$), whereas the plant transfer function $G(z^{-1})$ will be obtained by identification.

3.2. Controller design constraints

Using this block diagram (Fig. 6), stability and performance requirements can now be expressed by means of constraints on the closed-loop sensitivity functions (Landau et al., 1997). These constraints will be used for controller design and for performance analysis. They are guidelines for the controller synthesis and if it is shown that it is not be possible to fulfill all of them at the same time, a trade-off will exist between measurement and control performance. The sensitivity functions are defined by the following relations (cf. arrows on Fig. 6):

$$\mathbf{S}(z^{-1}) = 1/(1 + K \cdot G(z^{-1})), \tag{7}$$

$$\mathbf{SG}(z^{-1}) = G(z^{-1}) \cdot \mathbf{S}(z^{-1}), \quad \mathbf{KS}(z^{-1}) = K(z^{-1})\mathbf{S}(z^{-1}),$$

$$\mathbf{T}(z^{-1}) = K \cdot G(z^{-1})/(1 + K \cdot G(z^{-1})). \tag{8}$$

The output sensitivity function $\mathbf{S}$ characterizes the influence of an output disturbance on the closed-loop system output. The complementary sensitivity function $\mathbf{T}$ is the transfer from the reference signal $r(z^{-1})$ to the closed-loop system output $y_1(z^{-1})$. $\mathbf{KS}$ is the input sensitivity function and characterizes the influence of an output disturbance on the control signal $u(z^{-1})$. $\mathbf{GS}$ is the output sensitivity function with respect to an input disturbance.

3.2.1. Stability margins

In order to ensure sufficient stability margins, some limitation constraints must be imposed on the closed-loop sensitivity functions (Landau, 1990; Skogestad & Postlethwaite, 1996), the usual ones being on $\mathbf{S}$ and $\mathbf{T}$. The maximum $\|\mathbf{S}\|_\infty$ of the sensitivity function $\mathbf{S}$ should be less than 6 dB (9). The related graphical constraint is denoted Constraint 1 on Fig. 8. In the same manner, the complementary sensitivity function maximum $\|\mathbf{T}\|_\infty$ should be less than 3.5 dB (10) (Constraint 2). Moreover, Constraint 3 on the sensitivity $\mathbf{KS}$ (11) has been added in order to prevent instability due to saturation effects in the electronic part (digital computation overflow)

$$\|\mathbf{S}(z^{-1})\|_\infty \leqslant 6 \, \text{dB}, \tag{9}$$

$$\|\mathbf{T}(z^{-1})\|_\infty \leqslant 3.5 \, \text{dB}, \tag{10}$$

$$\|\mathbf{KS}(z^{-1})\|_\infty \leqslant 15 \, \text{dB}. \tag{11}$$

3.2.2. Measurement performance

The measurement performance specifications of Table 1 can also be formulated as inequalities to be respected by the closed-loop sensitivity functions.

Measurement Bandwidth: The closed-loop transfer function from the normalized external acceleration $p_1(z^{-1})$ to the sensor output $y_0(z^{-1})$ (Fig. 6) should have a constant gain for frequencies in the measurement bandwidth ($f \leqslant f_1$). Since design choice and calibration will impose that $|G_{d_1}(z^{-1})| = 1$ in this frequency range, this requirement is represented by (12) and Constraint 4 on Fig. 8.

$$|\mathbf{T}(z^{-1})| = 1, \quad 0 \leqslant f \leqslant f_1. \tag{12}$$

Measurement accuracy: The accuracy of the measurement system can be defined as the ratio between the magnitude of the measurement error signal $|\varepsilon_m(z^{-1})| = |y_0(z^{-1}) - p_1(z^{-1})|$ and the magnitude of the (normalized) input external acceleration $|p_1(z^{-1})|$ (Fig. 6). It means that the transfer function between p_1 and ε_m has to be considered. From Fig. 6, this transfer function is given by $\mathbf{S} \cdot G_{d1}$. According to Table 1, the magnitude of this transfer should remain under $-100 \, \text{dB}$ in the

measurement bandwidth:

$$|\mathbf{S} \cdot G_{d_1}(z^{-1})| \leqslant -100 \, \text{dB}, \quad 0 \leqslant f \leqslant f_1,$$

$$\Rightarrow |\mathbf{S}(z^{-1})| \leqslant -100 \, \text{dB}, \quad 0 \leqslant f \leqslant f_1. \tag{13}$$

It follows that constraint 5 on Fig. 8 should be respected.

Measurement linearity: As stated in Section 2.1, reducing the normalized proof mass displacement $y_2(z^{-1})$ to 1% (-40 dB) leads to a suitable SNDR. As a consequence, the transfer function from the normalized external acceleration $p_1(z^{-1})$ to the signal $y_2(z^{-1})$ ($\simeq$ normalized mass displacement x/x_{max}), which is equal to $\mathbf{SG} \cdot G_{d1}$, should respect the following constraint (Constraint 6 on Fig. 8):

$$|\mathbf{SG} \cdot G_{d_1}(z^{-1})| \leqslant -40 \, \text{dB}, \quad 0 \leqslant f \leqslant f_1,$$

$$\Rightarrow |\mathbf{SG}(z^{-1})| \leqslant -40 \, \text{dB}, \quad 0 \leqslant f \leqslant f_1. \tag{14}$$

Analog to digital conversion resolution: The two $\Sigma\Delta$ modulators introduce quantization noises, which are already properly shaped (high-pass noise transfer functions $G_{d_0}(z^{-1})$ and $G_{d_2}(z^{-1})$). In the measurement bandwidth, the loop must not enhance the amount of these noises in the output measurement signal y_0. It follows that the relations (15) and (16) must be respected

$$|\mathbf{KS}(z^{-1})| \leqslant 0 \, \text{dB}, \quad 0 \leqslant f \leqslant f_1, \tag{15}$$

$$|\mathbf{S}(z^{-1})| \leqslant 0 \, \text{dB}, \quad 0 \leqslant f \leqslant f_1. \tag{16}$$

Constraint 9 will stand for (15) and relation (16) is ignored since less constraining than relation (13).

3.2.3. Stability and performance robustness

Although stability margins, defined in Section 3.2.1, ensure a basic robustness, other robustness constraints can be specified in order to handle worst-case technological dispersions or time varying parameters. The first point would require the characterization of the uncertainties on the different physical parameters. Since this information is not available, this issue will be addressed later on, thanks to the identification approach and the controller programmability. In this prototyping step, robustness will only consider time varying parameters. The main parameter subject to time-variation will be the damping coefficient b in (6), through the modification of the air viscosity. At the operating conditions (Table 1), viscosity will be nearly insensitive to pressure variations. However, the viscosity dependence on temperature is not negligible. Indeed, the accelerometer should operate in a range of temperature from 0 to 85 °C and will be optimized for an ambient temperature of 27 °C. Using Sutherland's law (Gupta & Senturia, 1997) to model the temperature dependence of air viscosity, the worst cases will correspond to a decrease of 10% of the damping coefficient b or an increase of 15%. This variation can be modeled as a feedback uncertainty around the nominal plant (Doyle, Francis, &

Tannenbaum, 1992):

$$\tilde{G}(s) = G(s)/(1 + \Delta W_2 G(s)), \tag{17}$$

$$W_2(s) = \delta b \cdot s, \quad -1 \leqslant \Delta \leqslant 1, \tag{18}$$

where $W_2(s)$ provides the uncertainty profile and δb is the damping coefficient variation around the nominal value. The stability robustness condition for such an uncertainty model is (19), which leads to constraint (20) (Constraint 10 on Fig. 8):

$$\|W_2 GS(z^{-1})\|_\infty \leqslant 1, \tag{19}$$

$$\Leftrightarrow |GS(z^{-1})| \leqslant |W_2^{-1}(z^{-1})|, \quad \forall f, \tag{20}$$

with $W_2(z^{-1})$ so that $W_2(s) = 0 \cdot 15 \cdot b$.

Robustness toward this time varying parameter will also be checked after the controller design procedure: the closed-loop sensitivity functions will be identified on the complete system (Fig. 5) subject to the worst case variations of the damping coefficient and it will be verified if, in these operating conditions, the stability constraints (Constraints 1, 2 and 3) and the performance constraints (Constraints 4, 5, 6 and 9) are still respected.

4. Plant model identification and controller design

In the previous section, the control problem was formulated and the measurement specifications were turned into control loop performance specifications. This section presents the identification process and the control design methodology, applied to the complete simulation model (Fig. 5). The control and measurement performance is then analyzed. The aim of this section is to validate the methodology and to determine the achievable control and measurement performance.

4.1. Identification

In order to validate the identification process in simulation, the identification of the plant transfer function $G(z^{-1})$ was performed in open-loop, between input $u(z^{-1})$ and output $y_1(z^{-1})$ (Fig. 5). The excitation signal proposed for identification is a pseudo random binary sequence (PRBS) (Landau, 1990) whose characteristics are gathered in Table 3. Using the Matlab® identification toolbox, the

Table 3
PRBS characteristics

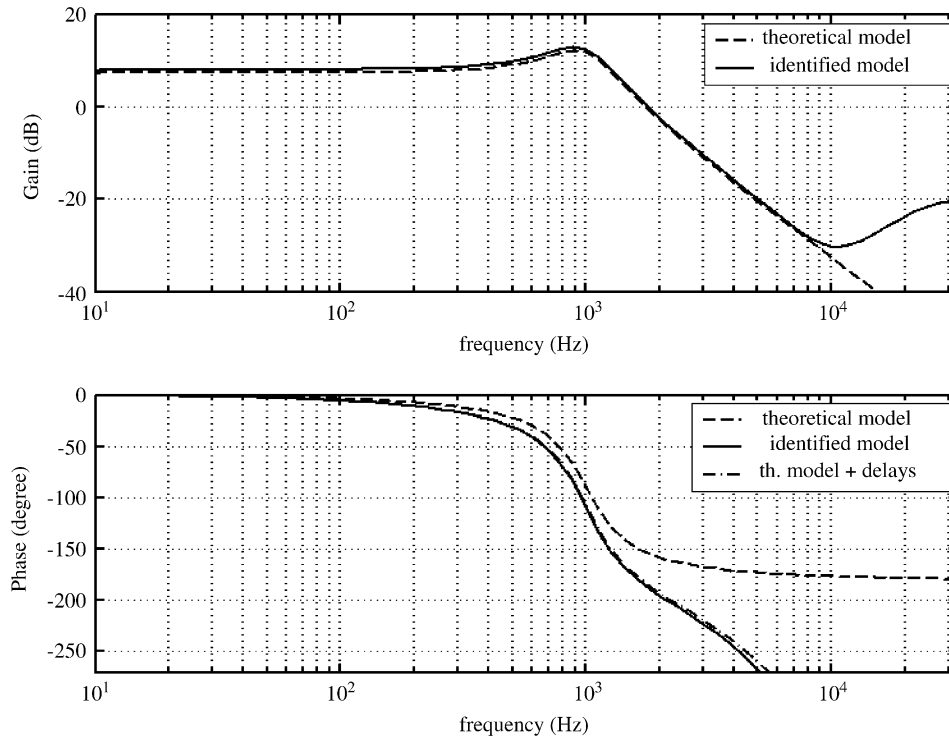| Parameter	Value
Sampling frequency	$f_{s_1} = 62.5 \, \text{kHz}$
Number of registers	$n_R = 16$
Frequency divider ratio	$\kappa = 4$
Number of periods	$N_{per} = 1$
Length (number of samples)	$L_{PRBS} = 262\,140$
Duration (real time)	$4.19 \, \text{s}$

Fig. 7. Bode diagram of the transfer function $G(z^{-1})$ (solid line) identified in simulations and of the theoretical model (dashed line). The dashed dot line represents theoretical model phase fitting, including additional delays.

best fit was obtained with a 4th order ARMAX model. The magnitude of the Bode plot of this identified model (Fig. 7) is in good accordance with the physical model of mass dynamics (6) multiplied by the capacitance readout gain K_{cs}. Phase plots can be matched by adding the delays induced by the electronic part ($\Sigma\Delta$ converters and up/down sampling filters) to the physical model.

4.2. Controller design

An *RS*-type controller was designed using the pole placement with sensitivity function shaping method described in Landau et al. (1997). This method has several advantages. It provides an instantaneous view of the expected sensor and control loop performance, so that the compromise between stability and measurement performance can be easily checked. Furthermore, the designer sets the controller order by choosing the fixed polynomial degrees, so that no controller order reduction method is needed. In this study, the maximum order of the controller is imposed by the electronics and controller synthesis must provide an 8th order controller (or lower).

The controller was designed so that the closed-loop natural frequency (f_3) remains the same as the open-loop one (f'_2) (closed-loop dominant poles P_D such that $f_3 \simeq f'_2 = 993$ Hz, with $\zeta = 0.8$ as damping coefficient). The other design characteristics are:

- *Controller fixed parts H_S*: The controller was designed imposing an integrator and a 2nd order filter ($f_n =$ 60 Hz, $\zeta = 0.1$) in order to fully reject the DC perturbations and to greatly reduce other perturbations in the measurement bandwidth.
- *Closed-loop auxiliary poles P_F*: In order to comply with stability Constraints 1 and 2, four high frequency multiple real poles were added around 13.6 kHz, as well as two complex pole pairs ($f_n = 1228$ Hz, $\zeta = 0.4$ and $f_n = 1310$ Hz, $\zeta = 1$).
- *Controller fixed parts H_R*: In order to comply with Constraint 3, one controller zero was imposed around 28 kHz.

These design choices result in a 7th order controller. The sensitivity functions are plotted in Fig. 8 and closed-loop performance is discussed in the next paragraph.

4.3. Control loop performance analysis

Measurement performance specifications trade-off with stability margins requirements, so that it was not possible to satisfy all the controller design constraints. The above controller was designed in order to comply as closely as possible with the measurement performance specifications given in Table 1, while stability and robustness constraints were relaxed. Fig. 8 plots in gray the nominal sensitivity functions using the identified model and the designed controller transfer function (Fig. 6) and, in black dashed lines, the sensitivity functions identified in closed-loop on the complete simulation model (Fig. 5). The discussion on
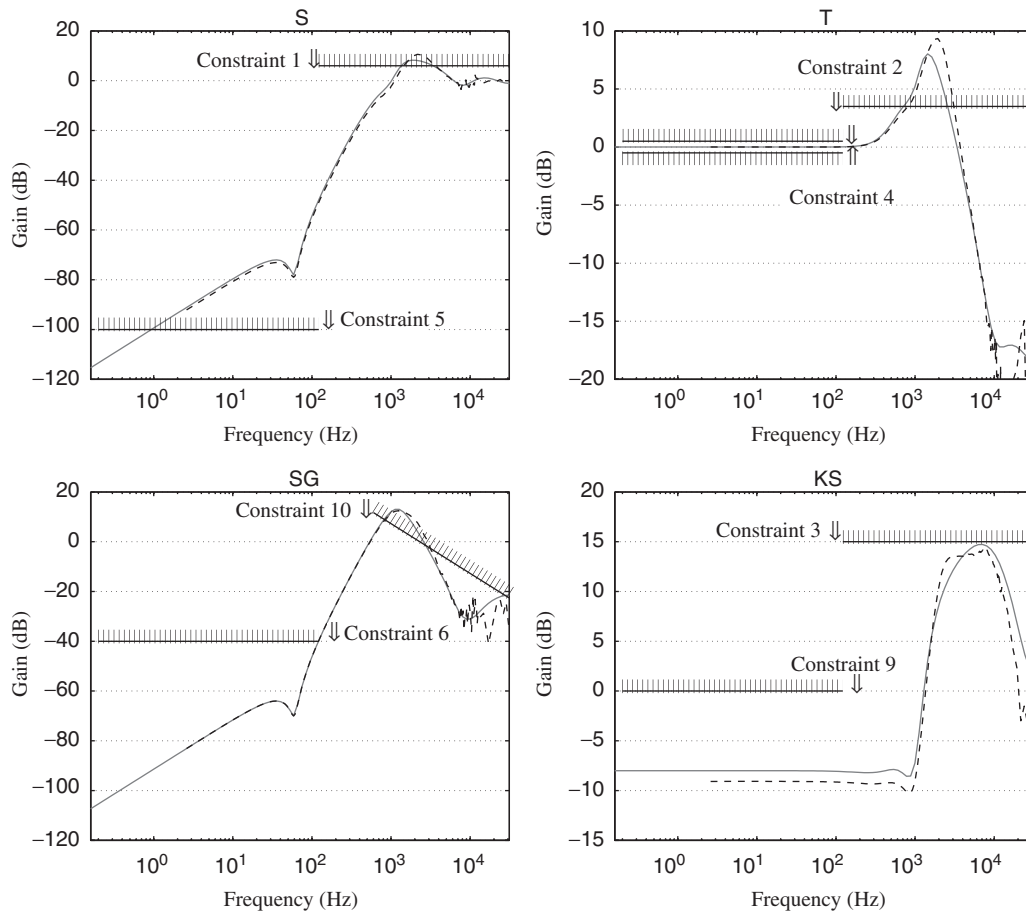
Fig. 8. Sensitivity functions and constraints: sensitivity functions calculated with the linear identified model are in gray lines while those identified on the realistic Simulink® model (including nonlinearity, filter blocks at f_{s_2},...) are in black dashed lines.

the achieved measurement and control performance trade-off is given below.

Constraints 1, 2 and 3 are not met but the stability margins are acceptable. Indeed, the maxima of the sensitivity function and of the complementary sensitivity function are equal to 8 dB, which is high but acceptable (Gain Margin (GM) $\geqslant 4.4$ dB, Phase Margin (PM) $\geqslant 22.8°$ guaranteed (Skogestad & Postlethwaite, 1996)). The maxima of the sensitivity functions identified in closed loop on the complete simulation model (Fig. 8, dashed lines) are higher than the designed ones ($\|S\|_\infty = 10.6$ dB, $\|T\|_\infty = 9.35$ dB), so that stability margins of the real system may be lower than expected (GM $\geqslant 3$ dB, PM $\geqslant 19.6°$). Bandwidth, linearity and noise shaping constraints (4, 6 and 9) are respected, so that the sensor system should fulfill linearity (THD) and analog to digital conversion resolution requirements (SQNR). Unfortunately Constraint 5, which concerns measurement accuracy, could not be respected: the measurement accuracy specification is too restrictive so that the performance and stability constraints cannot be both fulfilled. Nevertheless, the system displays good accuracy results: according to the **S** sensitivity function plot, the measurement accuracy is expected to be over 100 dB for acceleration frequencies below 1 Hz. It decreases for increasing acceleration frequencies: 72 dB for a 70 Hz signal bandwidth, 55 dB for the specified measurement bandwidth (122 Hz).

Finally, stability robustness toward damping coefficient variations with temperature is not theoretically proved since Constraint 10 is not fulfilled. The maximum damping coefficient variation δb is in fact equal to 6.3% of the damping coefficient's nominal value. This means that stability robustness is ensured for operating temperatures varying from 3 to 52 °C. Nevertheless, the system has been simulated for the worst-case temperature (0 and 85 °C) and the system was stable in both cases. Closed-loop sensitivity functions were identified for these two operating conditions. They showed that stability margin is decreased ($\|S\|_\infty = 11.2$ dB, $\|T\|_\infty = 10.4$ dB, GM $\geqslant 2.8$ dB, PM $\geqslant 17.4°$) for the lower temperature, while increased for the higher one. For frequencies under 122 Hz, sensitivity functions are identical, showing measurement performance robustness.

In order to guarantee stability, better stability margins were chosen for the real sensor.

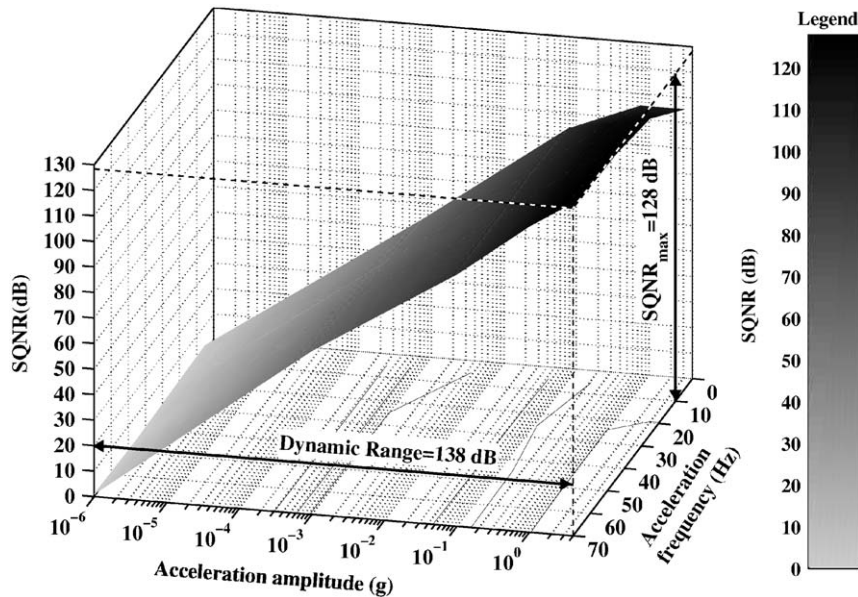The measurement performance expected from the sensitivity function analysis can be retrieved by temporal

Fig. 9. Measurement signal to quantification noise ratio (SQNR).

simulations on the physical model and computations on the measurement output spectrum. Fig. 9 plots, for different amplitude/frequency couples, the SQNR achieved by the measurement system in simulation and for the ideal model (without electronic part imperfections). According to sigma-delta theory, the SQNR presents a linear evolution versus increasing amplitude on a logarithmic scaled curve plot. This ideal model shows a maximum SQNR of 128 dB for $4g$ acceleration input. The smallest detectable signal amplitude is equal to $10^{-6}g$ (zero crossing point on Fig. 9) and the dynamic range is over 130 dB. The total harmonic distortion (THD) remains under the quantization noise floor. For a model including all noise sources and imperfections (thermal noise, slew rates, ...), the maximum SQNR equals 100 dB, while the THD remains under -110 dB. The minimum detectable acceleration equals $20\mu g$, leading to a 100 dB dynamic range.

5. Real sensor

Prototypes of the presented microsensor were realized and overview of the circuit performance and the controller design have been published in Condemine et al. (2005) and Soen, Voda, and Condemine (2005), respectively. The open-loop behavior of the sensor prototypes differs compared with theoretical and simulation models. Indeed, the fabricated mechanical part was different than expected — especially the effective capacitance gaps, which affect the cutoff frequency, the damping coefficient, the actuation gain and the readout gain, as well as the possible settings of the electronic part (sampling frequencies, feedback voltage, etc.). Fig. 10 compares the open-loop transfer function of the expected sensor with the one identified for a particular setting of the real sensor. A controller design, based on this identified model, was realized. Resulting sensitivity func-

tions are given in Fig. 11. The maxima of the sensitivity function **S** and **T** equal 7 and 6.5 dB, so that a 5.1 dB (23°) of gain (phase) margin is expected. The controller was tested on six different MEMS/integrated circuit couples and all were stable. **SG** and **S** sensitivity functions show that, for this design, the optimal bandwidth to consider for measurement performance is 0–25 Hz. In this bandwidth, the **KS** sensitivity function is equal to 2 dB due to the weak open-loop gain. As a consequence, the loop slightly deteriorates the initial quantization noise shaping. The **SG** sensitivity forecasts excellent measurement linearity, even higher than initial requirements ($THD \leqslant -100$ dB), while measurement error is expected to be around 0.1% ($S \leqslant -59$ dB). The designed accelerometer is in the state of the art of current commercial integrated capacitive accelerometers. A comparison is given in Soen et al. (2005). Further work (enhancement of capacitance readout circuit performance, mechanical part design and fabrication) are being performed in order to reach and overtake the initial measurement performance specifications of Table 1.

6. Conclusion

This paper details the design of a fully integrated control loop for a micromachined accelerometer using an advanced control strategy. First of all, the open-loop measurement system is briefly presented, pointing out its performance limitation due to the capacitive sensing nonlinearity. In order to achieve the linearity requirements, a closed-loop measurement system was chosen and the physical model of the corresponding *plant to be controlled* is given. Control and electronic design issues are taken into account in order to design the control/sensor loop architecture. Finally, the specific integrated circuit of the microsystem includes a programmable digital controller and provides the inputs
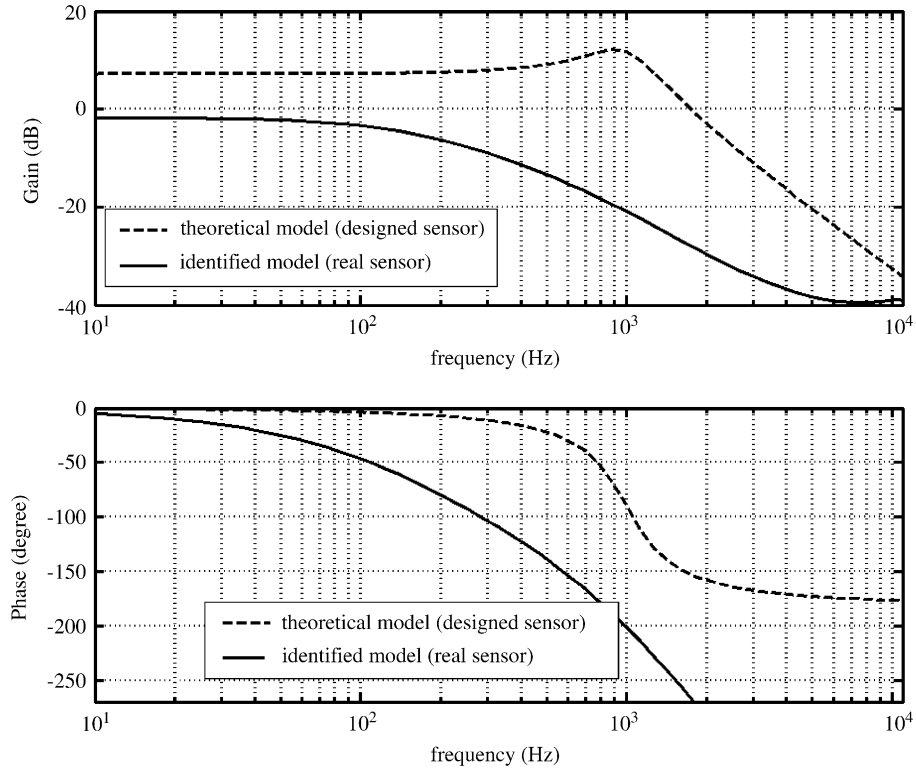
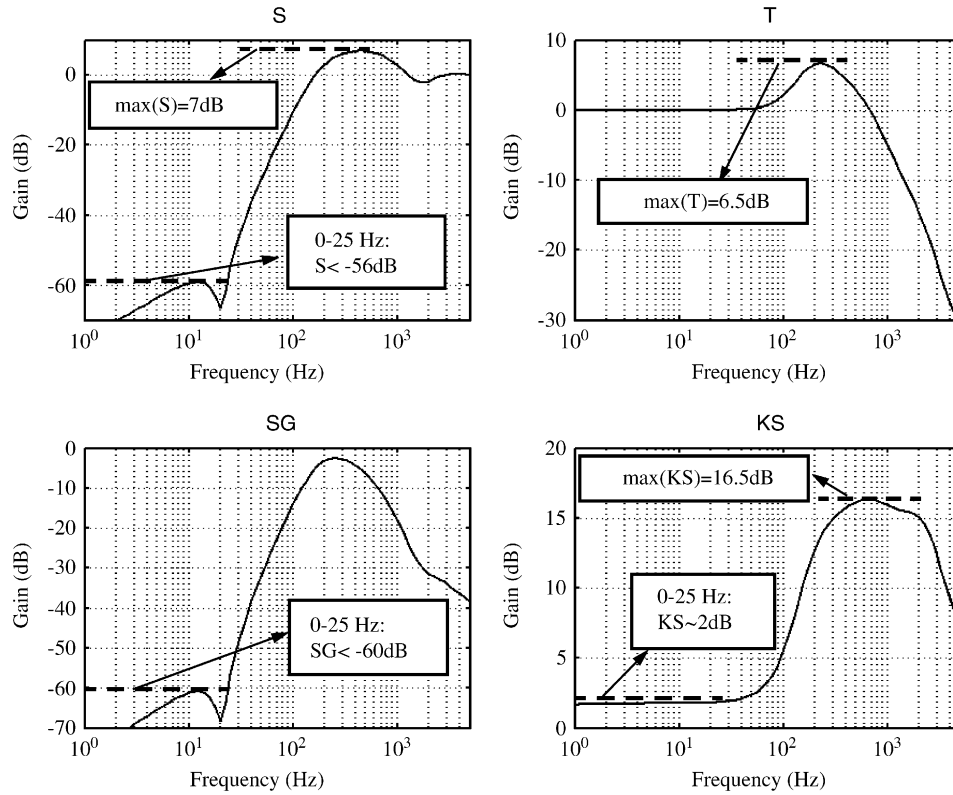Fig. 10. Bode diagram of the designed and real sensor in open loop.

Fig. 11. Closed-loop sensitivity functions of real sensor.

and outputs required for the identification of the effective plant model. Measurement requirements are translated into control requirements and a combined pole placement/sensitivity function shaping method is applied for the controller design. The identification/controller design procedure is performed on the complete simulation model. The identified model is similar to the theoretical one, and the measurement performance achieved by a 7th order controller nearly reaches the initial requirements. This procedure was successfully applied to the first prototypes despite the fact that their open-loop behavior differs from that expected. Real sensor performance depends on the circuit settings, the controller and the considered measurement bandwidth.

Acknowledgment

References

Chau, K. H.-L., et al. (1996). An integrated force-balanced capacitive accelerometer for low-g applications. *Sensors and Actuators A*, *54*, 472–476.

Condemine, C., et al. (2005). A 0.8 mA 50 Hz 15b SNDR $\Sigma\Delta$ closed-loop 10g accelerometer using an 8th-order digital compensator. *Proceedings of the 2005 IEEE international solid-state circuits conference* (Vol. 13, pp. 248–249). San Francisco.

Doyle, J. C., Francis, B. A., & Tannenbaum, A. R. (1992). *Feedback control theory*. Maxwell Macmillan Intern. Editions.

Gupta, R. K., & Senturia, S. D. (1997). Pull-in time dynamics as a measure of absolute pressure. *Proceedings of the IEEE 10th international workshop on MEMS* (pp. 290–294).

Handtmann, M., Aigner, R., Meckes, A., & Wachutka, G. K. M. (2002). Sensitivity enhancement of MEMS inertial sensors using negative springs and active control. *Sensors and Actuators A*, *97–98*, 153–160.

Kraft, M. (1997). *Closed-loop digital accelerometer employing oversampling conversion*. Ph.D. dissertation, Coventry University, School of Engineering, UK.

Landau, I. D. (1990). *System identification and control design*. Englewood Cliffs, NJ: Prentice-Hall Inc.

Landau, I. D., Lozano, R., & M'Saad, M. (1997). *Adaptive control*. London: Springer.

Liu, C., Rockstad, H. K., & Kenny, T. W. (1999). Robust controller design via μ-synthesis for high-performance micromachined tunneling accelerometer. *Proceedings of the 1999 American control conference* (pp. 247–252). San Diego.

Senturia, S. D. (2001). *Microsystem design*. Boston, Dordrecht, London: Kluwer Academic Publishers.

Skogestad, S., & Postlethwaite, I. (1996). *Multivariable feedback control: Analysis and design*. New York: Wiley.

Soen, J., Voda A., & Condemine C. (2005). Control strategy for measurement performance enhancement of a micromachined accelerometer. *16th IFAC world congress*, Prague.

Wang, B., Kajita, T., Sun, T., & Temes, G. C. (1998). New high-precision circuits for on-chip capacitor ratio testing and sensor readout. *Proceedings of the 1998 IEEE international symposium on circuits and systems* (Vol. 1, pp. 547–550).

Yazdi, N., Ayazi, F., & Najafi, K. (1998). Micromachined inertial sensors. *Proceedings of the IEEE*, *86*(8), 1640–1658.